# Quantum gyroscopes based on double-mode surface-acoustic-wave cavities

Yuting Zhu,[1,2,3] Shibei Xue,[1,2,3,*] Fangfang Ju,[5] and Haidong Yuan[4]

[a] *Department of Automation, Shanghai Jiao Tong University, Shanghai 200240, People's Republic of China*

[b] *Key Laboratory of System Control and Information Processing, Ministry of Education of China, Shanghai 200240, People's Republic of China*

[c] *Shanghai Engineering Research Center of Intelligent Control and Management, Shanghai 200240, People's Republic of China*

[d] *Department of Mechanical and Automation Engineering, The Chinese University of Hong Kong, Shatin, Hong Kong SAR, People's Republic of China*

[e] *School of Physics and Electronics, Hunan Normal University, Changsha 410081, People's Republic of China*

(Received 18 January 2024; revised 7 June 2024; accepted 9 July 2024; published 24 July 2024)

Recent progress shows that a surface-acoustic-wave (SAW) cavity can not only induce quantum acoustic dynamics, but can also form optomechanical-like systems. Its operating frequencies in the microwave band make it resistant to the thermal noise of surrounding environments, while its radiation-pressure couplings make it susceptible to weak forces. Based on these advantages, we propose a gyroscope comprising coupled microwave-SAW cavities. In this paper we systematically consider the range, signal-to-noise ratio, and sensitivity, which are the three most important indices to gyroscopes, but only partially considered in existing works. Additionally, we establish the fundamental limits of sensitivity when the quantum input is in the vacuum state and the squeezed vacuum state. We find that squeezing improves sensitivity and can surpass the standard quantum limit. However, this improvement can only reach up to $\sqrt{2}/2$ even as the squeezed parameter approaches infinity, which is rarely noted in recent works. Finally, we also offer analytical constraints for cooperativity and squeezed parameters. These constraints can be utilized to design gyroscopes based on coupled cavities in experiments.

DOI: 10.1103/PhysRevApplied.22.014061

## I. INTRODUCTION

Gyroscopes have made significant contributions to humankind as sensors for measuring angular velocity since they were first proposed by Foucault in 1852. However, measuring an extremely weak angular velocity, especially one much smaller than the Earth's rotation, poses great challenges for classical gyroscopes such as rigid rotator gyroscopes [1,2], mircoelectromagnetic gyroscopes [3,4], and Sagnac laser gyroscopes [5]. These classical gyroscopes struggle to meet the sensitivity and scalability requirements of modern gyroscopes. This directs scientists' attention to quantum gyroscopes, such as atom interferometer gyroscopes [6–19], nuclear magnetic resonance gyroscopes [20–23], and optomechanical gyroscopes [24–28], as quantum devices are more susceptible to interacted perturbations [29–34].

Among the above quantum gyroscopes, the optomechanical gyroscope stands out for not requiring the construction of magneto-optical trapping [7,9,11–16] or a vapor chamber [20–23] to trap ions or atoms. This feature makes it highly suitable for on-chip integration compared to the other types of gyroscopes. Furthermore, optomechanical systems benefit from their susceptibility to weak forces because of their unique radiation-pressure coupling, which enables them to be almost ideal devices for designing quantum gyroscopes based on centrifugal forces [24] or Coriolis forces [25,26,35]. However, the susceptibility to weak forces and the low frequency of the mechanical mode (typically in the kilohertz to megahertz range [36]) also make optomechanical systems susceptible to thermal Langevin forces, which restrict further improvements in sensitivity. For instance, a recent study shows that the sensitivity decreases by approximately 6 orders of magnitude when the temperature increases from 0 to 300 K [25]. Fortunately, emerging surface-acoustic-wave (SAW) cavities offer a potential solution to overcome this problem. The SAW cavity is a novel type of mechanical oscillator that operates in the microwave band and demonstrates exceptional quantum coherence [37–51]. In addition, SAW cavities can also be utilized for creating optomechanicalike systems with radiation-pressure couplings [46,47]. These advantages make SAW cavities not only retain the susceptibility to weak forces, but also immune to thermal Langevin forces, unlike the mechanical mode of

*Contact author: shbxue@sjtu.edu.cn

 

existing optomechanical systems. Therefore, they are superior devices for designing gyroscopes.

In addition to the devices, three crucial indices need to be taken into account when designing gyroscopes: (i) the range, which determines the interval within which the angular velocity can be detected; (ii) the signal-to-noise ratio (SNR), which determines whether the output signal can be readout; and (iii) the sensitivity, which determines the minimum detectable change of the angular velocity. These three indices are actually interrelated rather than independent of each other because they are constrained by the same parameters within a given system. Also, these indices are related to the noise of the system and are limited by the standard quantum limit [36,52], i.e., the minimum quantum noise allowed by the Heisenberg uncertainty relation. However, in recent proposals [18,19,24,26–28], the authors either only consider a portion of the above indices or fail to take into account the limitation imposed by the standard quantum limit. For instance, in recent atom interferometer gyroscopes [18,19], the authors only consider the influence of quantum input noise, but neglect other coherent quantum noise sources such as thermal Langevin noises. As a result, the best sensitivity obtained only applies to ideal cases that are not constrained by standard quantum limits. In recent optomechanical gyroscopes [24,27], the authors only consider the readable condition SNR $\geq 1$, but this condition actually determines the range of the angular velocity rather than sensitivity. In Ref. [28], the authors fail to consider the readable condition SNR $\geq 1$, although they skillfully employ coherent quantum noise cancelation to break the limitation on output noise imposed by the standard quantum limit. In Ref. [26], the authors use normal-mode splitting to measure angular velocity. However, this method only provides the range of the angular velocity. Therefore, recent proposals for quantum gyroscopes are incomplete.

To the above ends, we propose a quantum gyroscope utilizing SAW cavities and systematically take all three essential indices into account to overcome the problems mentioned above. Also, we discuss the fundamental limits of sensitivity in detail when the input is the vacuum state and squeezed vacuum state. As a result, the sensitivity is limited by the standard quantum limit when the input is in the vacuum state, and this limit can be surpassed after squeezing. More importantly, squeezing also has a limit to the improvement in sensitivity, and this limit is $\sqrt{2}/2$. However, this crucial result is rarely noted in recent works [18,19,24–28]. Furthermore, we provide analytical constraints on the cooperativity and the squeezed parameter, which would be beneficial for experiments.

The remainder of this paper is organized as follows. In Sec. II, we provide the model of the gyroscope and the equations of motion according to the quantum Langevin equation. We then analyze its range, SNR, sensitivity, and standard quantum limit under resonant driving in Sec. III.

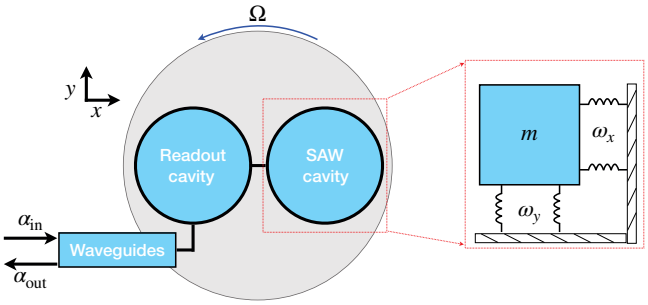


FIG. 1. Schematic of the quantum gyroscope. The system consists of two coupled cavities, where the SAW cavity acts as a mechanical oscillator having the $x$ and $y$ modes, as shown in the red box. These two modes couple to each other via the rotation of the platform with an unknown angular velocity $\Omega$, forming a basic gyroscope scheme in the $x$-$y$ plane. In addition, the $x$ mode also couples to a readout cavity (microwave band) that is connected to a waveguide. This allows the unknown angular velocity $\Omega$ to be readout through the output $\alpha_{\text{out}}$ using homodyne detection.

In Sec. IV, we provide the corresponding numerical simulations. Also, we focus on two issues that may be of concern in Sec. V: the calibration of the output signal and the affects induced by nonresonant driving. Finally, we conclude this work in Sec. VI.

## II. QUANTUM GYROSCOPE AND ITS LANGEVIN EQUATIONS

The quantum gyroscope being studied is based on previous optomechanical gyroscopes [24,25,27,28]. It consists of two coupled cavities fixed on a platform that rotate with an unknown angular velocity $\Omega$, as shown in Fig. 1. The SAW cavity acts as a double-mode mechanical oscillator with an effective mass $m$ and two operating frequencies $\omega_x$ and $\omega_y$, as depicted in the red box in Fig. 1. Hereafter, the subscripts $x$ and $y$ are used to label corresponding quantities in the $x$ and $y$ directions, respectively. Also, a readout cavity operating in the microwave band connected to a waveguide is used for homodyne detection. Our aim is to readout the angular velocity $\Omega$ of the platform through the output $\alpha_{\text{out}}$ in the waveguide.

The Hamiltonian of our system in terms of bosonic creation and annihilation operators reads

$$H = H_a + H_m + H_I \tag{1}$$

with

$$H_a = \hbar\omega_a a^\dagger a - i\hbar\sqrt{\kappa}(a^\dagger \alpha_{\text{in}} e^{-i\omega_d t} - \text{H.c.}), \tag{2a}$$

$$H_m = \hbar\omega_x\left(b_x^\dagger b_x + \tfrac{1}{2}\right) + \hbar\omega_y\left(b_y^\dagger b_y + \tfrac{1}{2}\right) + \frac{i\hbar\Omega}{2}[\eta_1(b_x^\dagger b_y - b_x b_y^\dagger) + \eta_2(b_x^\dagger b_y^\dagger - b_x b_y)] \tag{2b}$$

$$H_I = -i\hbar g_1(b_x a^\dagger - b_x^\dagger a) + i\hbar g_2(b_x a - b_x^\dagger a^\dagger). \tag{2c}$$

Here $H_a$ represents the Hamiltonian of the readout cavity driven by the input $\alpha_{\rm in} = \alpha + a_{\rm in}$, where $N_{\rm in} = |\alpha|^2$ represents the input photon number and $a_{\rm in}$ refers to the corresponding quantum input [52]. If the quantum input $a_{\rm in}$ is in a vacuum state, the driving $\alpha_{\rm in}$ actually represents a coherent state input [53]. Operator $H_m$ represents the Hamiltonian of the double-mode SAW cavity with the coefficients $\eta_1 = \sqrt{\omega_x/\omega_y} + \sqrt{\omega_y/\omega_x}$ and $\eta_2 = \sqrt{\omega_x/\omega_y} - \sqrt{\omega_y/\omega_x}$ (see the Appendix for more details). The two initially isolated modes become coupled to each other when the platform is rotating, forming a basic gyroscope scheme in the $x$-$y$ plane. Without loss of generality, Hamiltonian $H_m$ considered here is a complete form including centrifugal forces that are neglected in previous work [27] (see the Appendix for further details). Hamiltonian $H_I$ denotes the interaction between the readout cavity and the $x$ mode of the SAW cavity. The first term corresponds to a beam-splitter coupling, while the second term represents a down-conversion coupling [54]. When the coupling strength $g_1 = g_2$, the interaction Hamiltonian $H_I$ reduces to a linearized optomechanical coupling $i\hbar g(a - a^\dagger)(b_x + b_x^\dagger)$ [36,52]. For brevity, we consider $\omega_x = \omega_y = \omega_b$ and $g_1 = g_2 = g$ in the following.

In a rotating frame with respect to the driving frequency $\omega_d$, the quantum Langevin equations of the system read

$$\dot{a} = \left(i\Delta - \frac{\kappa}{2}\right)a - g(b_x + b_x^\dagger) - \sqrt{\kappa}\alpha_{\rm in}, \tag{3a}$$

$$\dot{b}_x = \left(-i\omega_b - \frac{\gamma_x}{2}\right)b_x + g(a - a^\dagger) + \Omega b_y - \sqrt{\gamma_x}f_x, \tag{3b}$$

$$\dot{b}_y = \left(-i\omega_b - \frac{\gamma_y}{2}\right)b_y - \Omega b_x - \sqrt{\gamma_y}f_y, \tag{3c}$$

where the detuning between the readout cavity and the driving is $\Delta = \omega_d - \omega_a$, and $\gamma_{x(y)}$ is the decay rate of the $x(y)$ mode due to the thermal noise $f_{x(y)}$. The thermal noises satisfy the correlations [47]

$$\begin{aligned}
&\langle f_{x(y)}(t)\rangle = 0,\\
&\langle f_{x(y)}^\dagger(t) f_{x(y)}(t')\rangle = n_{\rm th}\delta(t - t'),\\
&\langle f_{x(y)}(t) f_{x(y)}^\dagger(t')\rangle = (n_{\rm th} + 1)\delta(t - t'),
\end{aligned}$$

where $n_{\rm th} = [\exp(\hbar\omega_b/k_B T) - 1]^{-1}$ is the equilibrium mean thermal phonon number of the SAW cavity. In the state-of-the-art SAW-superconducting-circuit experiments [46,47], the temperature of the surrounding environment can reach the milikelvin regime inside a dilution refrigerator, and the frequency of the SAW cavity $\omega_b$ can be enhanced to gigahertz. Therefore, one can let $n_{\rm th} = 0$. Furthermore, the corresponding input-output relation is given by

$$\alpha_{\rm out}(t) = \alpha_{\rm in}(t) + \sqrt{\kappa}a(t). \tag{4}$$

The equations of motion (3a)–(3c) can be easily solved using Fourier transformations $O(\omega) = \int {\rm d}t\, O(t)e^{i\omega t}$ and $O^\dagger(\omega) = \int {\rm d}t\, O^\dagger(t)e^{i\omega t} = [O(-\omega)]^\dagger$. With the dimensionless position operator $X = b_x + b_x^\dagger$, the solution of Eqs. (3a)–(3c) reads

$$a(\omega) = \chi_a(\omega)[\sqrt{\kappa}\alpha_{\rm in}(\omega) + gX(\omega)], \tag{5}$$

$$\begin{aligned}
X(\omega) = {}& P_1(\omega)\alpha_{\rm in}(\omega) + P_1^*(-\omega)\alpha_{\rm in}^\dagger(\omega)\\
&+ P_2(\omega)f_x(\omega) + P_2^*(-\omega)f_x{}^\dagger(\omega)\\
&+ P_3(\omega)f_y(\omega) + P_3^*(-\omega)f_y{}^\dagger(\omega)
\end{aligned} \tag{6}$$

with

$$P_1(\omega) = -\frac{\kappa\sqrt{\gamma_x C_o}}{2}\frac{\chi_a(\omega)[\chi_x(\omega) - \chi_x^*(-\omega)]}{1 + i\tilde{\Delta}(\omega)[\chi_x(\omega) - \chi_x^*(-\omega)]},$$

$$P_2(\omega) = \frac{\sqrt{\gamma_x}\chi_x(\omega)}{1 + i\tilde{\Delta}(\omega)[\chi_x(\omega) - \chi_x^*(-\omega)]},$$

$$P_3(\omega) = -\frac{\sqrt{\gamma_y}\Omega\chi_x(\omega)\chi_y(\omega)}{1 + i\tilde{\Delta}(\omega)[\chi_x(\omega) - \chi_x^*(-\omega)]},$$

where the susceptibility functions of cavities are given by

$$\chi_a(\omega) = \frac{1}{i\omega + i\Delta - \kappa/2},$$

$$\chi_x(\omega) = \frac{i\omega - i\omega_b - \gamma_y/2}{(i\omega - i\omega_b - \gamma_x/2)(i\omega - i\omega_b - \gamma_y/2) + \Omega^2},$$

$$\chi_y(\omega) = \frac{1}{i\omega - i\omega_b - \gamma_y/2},$$

the modified detuning induced by the nonresonant driving is

$$\tilde{\Delta}(\omega) = 2g^2\Delta\chi_a(\omega)\chi_a^*(-\omega),$$

and the cooperativity [36,52] is defined as

$$C_o = \frac{4g^2}{\kappa\gamma_x}.$$

From the above equations, one can see that the $b_x$ mode couples to its conjugate mode $b_x^\dagger$ with a strength $\tilde{\Delta}(\omega)$ when the detuning $\Delta$ is not zero. This would slightly modify the result at $\Delta = 0$, as discussed later.

## III. HOMODYNE DETECTION AND PERFORMANCE OF THE GYROSCOPE

As a quantum gyroscope, we aim to readout the unknown angular velocity $\Omega$ and analyze the fundamental limits of performance indices permitted by quantum

mechanics. However, the angular velocity $\Omega$ is directly encompassed in the quadrature $X$, and it is then transferred to the output $\alpha_{\rm out}$ through coupling with the readout cavity. Therefore, we measure quadrature $X$ by observing the photon current $I = \alpha_{\rm out} + \alpha_{\rm out}^{\dagger}$. Actually, the quantum limit of the aforementioned homodyne detection occurs at the zero-detuned driving [52]. Within the existing optomechanical experiments, the frequency of the SAW cavity can be much lower than the damping of the readout cavity. For instance, $\kappa \sim$ KHz–MHz, $\omega_b \sim 10^{-6}$Hz–KHz, and $\gamma_{x,y} \sim 10^{-6}$ Hz–KHz in traditional optomechanics (see Table 2 of Ref. [36]); $\kappa \sim 3.5$ GHz, $\omega_b \sim 1.05$ GHz, and $\gamma_{x,y} \sim 10.5$ KHz in SAW-based optomechanics [47]. This allows the state of the readout cavity to adiabatically track the motion of the $x$ mode [52], and thus gives us a good approximation for the susceptibility function

$$\chi_a = \chi_a^* \equiv -\kappa/2. \tag{7}$$

In the following, this approximation runs until Sec. IV. We also discuss nonzero detuned cases in Sec. V as a comparison.

As we mentioned, there are three important indices for a gyroscope: the *range*, which determines the range within which the angular velocity $\Omega$ can be readout; the *SNR*, which determines whether the output signal can be read; and the *sensitivity* or *accuracy*, which determines the minimum detectable change of the angular velocity $\Delta\Omega$, similar to the ticks of a ruler. Therefore, the gyroscope is more sensitive when $\Delta\Omega$ is smaller. In this work, we use $\Delta\Omega^2$ as the sensitivity because the angular velocity always appears squared in all quantities. All of these indices are closely related to the power spectral density of the noise. Thereby, we first introduce the noise power spectral density and then discuss these indices in detail.

### A. Noise power spectral density and standard quantum limit

We now provide a general form of the noise power spectral density for an observable quantity $O$:

$$\begin{aligned} N_O(\omega) &= \int {\rm d}t\, e^{i\omega t}[\langle O(t)O(0)\rangle - \langle O(t)\rangle\langle O(0)\rangle] \\ &= \frac{1}{2\pi}\int {\rm d}\omega'\,[\langle O(\omega)O(\omega')\rangle - \langle O(\omega)\rangle\langle O(\omega')\rangle]. \end{aligned} \tag{8}$$

The first term on the right-hand side represents the sum of the quantum average and the statistical average, while the second term represents the statistical average alone. The physics behind Eq. (8) is explained by the Wiener-Khinchin theorem: the autocorrelation function of an observable quantity is connected to its power spectral density through a Fourier transformation [36]. The area under the spectral density equals the fluctuation of the quantity:

$$\frac{1}{2\pi}\int {\rm d}\omega\, N_O(\omega) = \langle O^2(0)\rangle - \langle O(0)\rangle^2. \tag{9}$$

Note that our definition (8) differs slightly from those in Refs. [36,52], since our input $\alpha_{\rm in}$ contains a classical amplitude $\alpha$ besides the quantum input $a_{\rm in}$. We refer the reader to Refs. [36,52] for more detail about the noise spectral density. In this work, we also consider the symmetric noise power spectral density $\bar{N}_O(\omega) = [N_O(\omega) + N_O(-\omega)]/2$.

#### *1. Quantum input $a_{\rm in}$ in the vacuum state*

Before we proceed, we now introduce the correlations of the quantum input $a_{\rm in}(\omega)$:

$$\langle 0|a_{\rm in}(\omega)|0\rangle = \langle 0|a_{\rm in}^{\dagger}(\omega)|0\rangle = 0, \tag{10a}$$

$$\langle 0|a_{\rm in}^{\dagger}(\omega)a_{\rm in}(\omega')|0\rangle = 0, \tag{10b}$$

$$\langle 0|a_{\rm in}(\omega)a_{\rm in}^{\dagger}(\omega')|0\rangle = 2\pi\delta(\omega+\omega'). \tag{10c}$$

According to definition (8), we can obtain the noise power spectral density

$$N_X(\omega) = N_X^{\rm zpf}(\omega) + N_X^{\rm ba}(\omega) + N_X^{\Omega}(\omega) \tag{11}$$

of quadrature $X$ using the above correlations, where the first term $N_X^{\rm zpf}(\omega) = \gamma_x|\chi_x(\omega)|^2$ is the zero-point noise caused by the thermal noise $f_x$ at zero kelvin, the second term $N_X^{\rm ba}(\omega) = \gamma_x C_o|\chi_x(\omega) - \chi_x^*(-\omega)|^2$ represents the back-action noise caused by the quantum fluctuation input $a_{\rm in}$, and the third term $N_X^{\Omega}(\omega) = \Omega^2\gamma_y|\chi_x(\omega)|^2|\chi_y(\omega)|^2$ denotes the angular noise induced by the thermal noise $f_y$. Furthermore, the total noise power spectral density of quadrature $X$ also includes imprecision noise resulting from the measurement [52], which is associated with the photon current

$$\begin{aligned} I(\omega) &= \alpha_{\rm out}(\omega) + \alpha_{\rm out}^{\dagger}(\omega) \\ &= -2\sqrt{\gamma_x C_o}X(\omega) - [\alpha_{\rm in}(\omega) + \alpha_{\rm in}^{\dagger}(\omega)]. \end{aligned} \tag{12}$$

We see that the photon current amplifies mode $x$ with a coefficient $G = 2\sqrt{\gamma_x C_o}$. Therefore, the noise power spectral density of the photon current should also include an amplification for $N_X(\omega)$, i.e.,

$$\begin{aligned} N_I(\omega) = 1 &+ 4\gamma_x C_o N_X(\omega) + 2\gamma_x C_o[\chi_x(\omega) + \chi_x^*(\omega) \\ &- \chi_x(-\omega) - \chi_x^*(-\omega)], \end{aligned} \tag{13}$$

where the constant term is the shot noise resulting from the autocorrelation of the quantum input $a_{\rm in}$ in Eq. (12), the second term represents the amplified $N_X(\omega)$, and the third

term denotes the noise resulting from the cross-correlation between quadrature $X$ and the quantum fluctuation input $a_{\rm in}$. Note that the third term in Eq. (13) cancels out in the symmetric form, i.e.,

$$\bar{N}_I(\omega) = 1 + 4\gamma_x C_o \bar{N}_X(\omega). \tag{14}$$

Therefore, the total noise power spectral density (symmetric) referred back to quadrature $X$ reads

$$\bar{N}_X^{\rm tot}(\omega) = \bar{N}_X^{\rm zpf}(\omega) + \bar{N}_X^{\rm add}(\omega) + \bar{N}_X^{\Omega}(\omega) \tag{15}$$

with the additional noise

$$\bar{N}_X^{\rm add}(\omega) = \bar{N}_X^{\rm ba}(\omega) + \bar{N}_X^{\rm im}, \tag{16}$$

where $\bar{N}_X^{\rm im} = 1/G^2$ is the imprecision noise mentioned before.

What we emphasized in Eq. (15) is that the total noise power spectral density is limited by the standard quantum limit $\bar{N}_X^{\rm add}(\omega) \geq \bar{N}_X^{\rm zpf}(\omega)$. In short, the standard quantum limit describes the minimum additional noise allowed by the Heisenberg uncertainty relation [36,52]. In addition, although both the angular noise $\bar{N}_X^{\Omega}(\omega)$ and the back-action noise $\bar{N}_X^{\rm ba}(\omega)$ result from the coupling between the $x$ mode and other modes, the back-action noise $\bar{N}_X^{\rm ba}(\omega)$ is absorbed into the additional noise $\bar{N}_X^{\rm add}(\omega)$, but not the angular noise $\bar{N}_X^{\Omega}(\omega)$. The reason is that the angular noise $\bar{N}_X^{\Omega}(\omega)$ is zero when $\Omega = 0$, but the back-action noise $\bar{N}_X^{\rm ba}(\omega)$ is not. Therefore, the angular noise $\bar{N}_X^{\Omega}(\omega)$ does not impose any limitations on the minimum total noise $\bar{N}_X^{\rm tot}(\omega)$.

Since the minimum total noise spectral density $\bar{N}_X^{\rm tot}(\omega)$ is obtained at $\omega = \omega_b$, we focus on this frequency and discuss the standard quantum limit in detail. Here, we consider the thermal decay rate $\gamma_{x(y)}$ to be much less than the mechanical frequency $\omega_b$, i.e., a low-damped mechanical oscillator, so that the noise power spectral densities can be approximated as

$$\bar{N}_X^{\rm zpf}(\omega_b) \approx \frac{\gamma_x}{2}\frac{\gamma_y^2/4}{(\gamma_x\gamma_y/4+\Omega^2)^2}, \tag{17a}$$

$$\bar{N}_X^{\rm add}(\omega_b) \approx \gamma_x C_o \frac{\gamma_y^2/4}{(\gamma_x\gamma_y/4+\Omega^2)^2} + \frac{1}{G^2}, \tag{17b}$$

$$\bar{N}_X^{\Omega}(\omega_b) \approx \frac{2\Omega^2}{\gamma_y}\frac{\gamma_y^2/4}{(\gamma_x\gamma_y/4+\Omega^2)^2}. \tag{17c}$$

One can easily check that

$$\bar{N}_X^{\rm add}(\omega_b) \geq \frac{\gamma_y/2}{\gamma_x\gamma_y/4+\Omega^2},$$

and the equality holds if and only if $C_o = (\gamma_x\gamma_y/4 + \Omega^2)/(\gamma_x\gamma_y)$. In doing so, we have

$$\begin{aligned}\bar{N}_X^{\rm add}(\omega_b) - \bar{N}_X^{\rm zpf}(\omega_b) &= \frac{1}{2}\frac{\gamma_y}{\gamma_x\gamma_y/4+\Omega^2} \\ &\quad\times\left(1 - \frac{1}{1+4\Omega^2/\gamma_x\gamma_y}\right) \\ &\geq \frac{1}{4}\frac{\gamma_y}{\gamma_x\gamma_y/4+\Omega^2}, \qquad \Omega \neq 0,\end{aligned}$$

and thus in this case we find that the system fails to reach the standard quantum limit when the platform is rotating.

Also, one can see that $\bar{N}_X^{\Omega}(\omega_b) \leq \bar{N}_X^{\rm zpf}(\omega_b)$ when $\Omega^2 \leq \gamma_x\gamma_y/4$. This implies that the angular noise $\bar{N}_X^{\Omega}(\omega_b)$ can be disregarded if the angular velocity $\Omega$ is sufficiently small. In other words, the additional noise $\bar{N}_X^{\rm add}(\omega_b)$ always dominates the total noise $\bar{N}_X^{\rm tot}(\omega_b)$. This corresponds to a very practical scenario: if the rotation of the platform is much less than that of the Earth (about $10^{-5}$ rad/s $\approx 10^{-6}$ Hz), the total noise $\bar{N}_X^{\rm tot}(\omega)$ is almost independent of the angular velocity $\Omega$ for mechanical oscillators with quality factors $Q \approx 10^3$–$10^5$ and operating frequencies in the kilohertz to megahertz range [36]. Therefore, it would be impossible to readout the angular velocity from the noise spectral density, as was done in Ref. [27]. In addition, in Ref. [27] the authors also ignore the constraints of the standard quantum limit on the total noise power spectral density $\bar{N}_X^{\rm tot}(\omega)$. Therefore, the assumption they considered, $\bar{N}_X^{\rm add}(\omega_b) \ll \bar{N}_X^{\rm zpf}(\omega_b)$, would not hold in experiments when the quantum input is in a vacuum state.

#### *2. Quantum input $a_{\rm in}$ in the squeezed vacuum state*

In this case, we consider $a_{\rm in}$ in a single-mode squeezed vacuum state

$$|\xi\rangle = S(\xi)|0\rangle = e^{-[\xi a_{\rm in}^\dagger(\omega)a_{\rm in}^\dagger(\omega) - \xi^* a_{\rm in}(\omega)a_{\rm in}(\omega)]/2}|0\rangle \tag{18}$$

with an arbitrary complex number $\xi = re^{i\phi}$, $r > 0$. Correspondingly, the correlations of the quantum input $a_{\rm in}$ are calculated as

$$\langle\xi|a_{\rm in}(\omega)|\xi\rangle = \langle\xi|a_{\rm in}^\dagger(\omega)|\xi\rangle = 0, \tag{19a}$$

$$\langle\xi|a_{\rm in}(\omega)a_{\rm in}^\dagger(\omega')|\xi\rangle = 2\pi\delta(\omega+\omega')\cosh^2 r, \tag{19b}$$

$$\langle\xi|a_{\rm in}^\dagger(\omega)a_{\rm in}(\omega')|\xi\rangle = 2\pi\delta(\omega+\omega')\sinh^2 r. \tag{19c}$$

In doing so, the symmetric noise spectral density of the photon current reads

$$\bar{N}_I(\omega) = e^{-2r} + 4\gamma_x C_o \bar{N}_X(\omega) \tag{20}$$

with

$$\bar{N}_X(\omega) = \bar{N}_X^{\rm zpf}(\omega) + e^{-2r}\bar{N}_X^{\rm ba}(\omega) + \bar{N}_X^{\Omega}(\omega), \tag{21}$$

where we have assumed that $\phi = \pi$ in the derivation to obtain an attenuated shot noise, i.e., the first term in Eq. (20). Accordingly, the total noise spectral density for the mechanical $x$ mode becomes

$$\bar{N}_X^{\rm tot}(\omega) = \bar{N}_X^{\rm zpf}(\omega) + \bar{N}_X^{{\rm add},s}(\omega) + \bar{N}_X^{\Omega}(\omega) \tag{22}$$

with the squeezed additional noise

$$\bar{N}_X^{{\rm add},s}(\omega) = e^{-2r}\bar{N}_X^{\rm ba}(\omega) + \bar{N}_X^{\rm im}. \tag{23}$$

Compared to Eq. (16), we see that the squeezed vacuum input causes the back-action noise $\bar{N}_X^{\rm ba}(\omega)$ to decrease exponentially, but it does not affect the imprecision noise $\bar{N}_X^{\rm im}$. This provides an opportunity to achieve or surpass the standard quantum limit. For a clear comparison, we also specialize to the frequency $\omega = \omega_b$, as in Sec. III A 1, and then we have

$$\bar{N}_X^{{\rm add},s}(\omega_b) \geq e^{-r}\frac{\gamma_y/2}{\gamma_x\gamma_y/4 + \Omega^2},$$

where the equality holds if and only if $C_o = e^r(\gamma_x\gamma_y/4 + \Omega^2)/(\gamma_x\gamma_y)$. At this time, we further obtain

$$\bar{N}_X^{{\rm add},s}(\omega_b) - \bar{N}_X^{\rm zpf}(\omega_b) \geq \frac{1}{2}\frac{\gamma_y}{\gamma_x\gamma_y/4 + \Omega^2} \times \left(e^{-r} - \frac{1}{2}\right), \qquad \Omega \neq 0,$$

so that the system can reach and even surpass the standard quantum limit [36,52] when the condition $r \geq \ln 2$ is satisfied.

Re-examining the noise spectral density from the perspective of the output, i.e., the noise spectral density $\bar{N}_I(\omega_b)$, we can easily find that the zero-point noise $\bar{N}_X^{\rm zpf}(\omega_b)$ dominates the noise spectral density $\bar{N}_I(\omega_b)$ when the conditions $r \to \infty$ and $\Omega^2 \leq \gamma_x\gamma_y/4$ are satisfied. If we consider the shot noise as the floor of the noise spectral density of the photon current under the vacuum input [cf. Eq. (14)], this floor approaches zero with squeezing. As a result, the noise spectral density $\bar{N}_I(\omega_b)$ depends only on the zero-point noise $\bar{N}_X^{\rm zpf}(\omega_b)$. In other words, the noise resulting from the quantum input $a_{\rm in}$ can be eliminated by squeezing, so that the system is only influenced by the zero-point noise $\bar{N}_X^{\rm zpf}(\omega_b)$. However, the shot noise always plays roles if the quantum input $a_{in}$ is not squeezed [cf. Eq. (14)], which is the major difference of noise power spectral densities between the two cases.

### B. Signal-to-noise ratio, range, and sensitivity

After introducing the noise spectral density in the previous section, we now analyze the range, SNR, and sensitivity of the gyroscope. Using correlations (10) and (19), we define the signal spectrum as

$$\begin{aligned} S(\omega) &= |\langle I(\omega)\rangle - \langle I(-\omega)\rangle|^2 \\ &= |2\gamma_x C_o[\chi_x(\omega) + \chi_x^*(\omega) \\ &\quad - \chi_x(-\omega) - \chi_x^*(-\omega)](\alpha - \alpha^*)|^2 \\ &= 16N_{\rm in}\gamma_x^2 C_o^2|\chi_x(\omega) + \chi_x^*(\omega) \\ &\quad - \chi_x(-\omega) - \chi_x^*(-\omega)|^2, \end{aligned} \tag{24}$$

where we set $\varphi = \arg\,\alpha = \pi/2$ for brevity. As the statistical average of the photon current, the output signal depends only on the susceptibility function of the system and is proportional to the input photon number. At the frequency $\omega = \omega_b$, it can be approximated as

$$S(\omega_b) \approx 16N_{\rm in}C_o^2\frac{\gamma_x^2\gamma_y^2}{(\gamma_x\gamma_y/4 + \Omega^2)^2}, \tag{25}$$

where we also assume that $(\Omega, \gamma_{x(y)}) \ll \omega_b$, as we did when deriving Eqs. (17a)–(17c). Once the gyroscope is designed, one can use this equation to readout the angular velocity $\Omega$ from the measured signal.

With the signal spectrum $S(\omega)$ and the noise spectral density $\bar{N}_I(\omega)$, one can easily write the SNR as

$${\rm SNR}(\omega) = \frac{S(\omega)}{\bar{N}_I(\omega)}. \tag{26}$$

When the quantum input $a_{\rm in}$ is in the vacuum state or the squeezed vacuum state, the SNR per photon can be approximated as

$$\frac{{\rm SNR}_v(\omega_b)}{N_{\rm in}} \approx \frac{16C_o^2\gamma_x^2\gamma_y^2/(\gamma_x\gamma_y/4 + \Omega^2)^2}{1 + C_o[C_o + 2(\gamma_x\gamma_y/4 + \Omega^2)/\gamma_x\gamma_y]\,\gamma_x^2\gamma_y^2/(\gamma_x\gamma_y/4 + \Omega^2)^2} \tag{27}$$

or

$$\frac{{\rm SNR}_s(\omega_b)}{N_{\rm in}} \approx \frac{16e^{2r}C_o^2\gamma_x^2\gamma_y^2/(\gamma_x\gamma_y/4 + \Omega^2)^2}{1 + C_o[C_o + 2(e^{2r}\gamma_x\gamma_y/4 + \Omega^2)/\gamma_x\gamma_y]\,\gamma_x^2\gamma_y^2/(\gamma_x\gamma_y/4 + \Omega^2)^2}, \tag{28}$$

where the subscripts $v$ and $s$ label the vacuum and the squeezed vacuum, respectively. It should be pointed out that the output signal can only be readout when the SNR per photon is greater than 1. The advantage of this is that the readability of the output signal does not depend on the pump power of the input field, but only relates to the system parameters. In doing so, it provides an upper bound for the angular velocity and a lower bound for the cooperativity. When the quantum input $a_{\rm in}$ is in the vacuum state, these bounds read

$$0 \leq \Omega_v^2 \leq \left(3C_o - \frac{1}{4}\right)\gamma_x\gamma_y \tag{29}$$

and

$$C_o \geq \tfrac{1}{12}. \tag{30}$$

When the quantum input $a_{\rm in}$ is in the squeezed vacuum state, they become

$$0 \leq \Omega_s^2 \leq \left(\sqrt{e^{4r}+16e^{2r}-1}C_o - e^{2r}C_o - \tfrac{1}{4}\right)\gamma_x\gamma_y \tag{31}$$

and

$$C_o \geq \frac{1}{4}\frac{1}{\sqrt{e^{4r}+16e^{2r}-1}-e^{2r}}. \tag{32}$$

One can easily check that conditions (31) and (32) reduce to conditions (29) and (30) when the squeezed parameter $r = 0$.

Upon completing the discussions on the range and the SNR, we now focus on the sensitivity [18,19,55], which is given by

$$\Delta\Omega^2(\omega) = \sqrt{\frac{\bar{N}_I(\omega)}{|\partial_{\Omega^2}[\langle I(\omega)\rangle - \langle I(-\omega)\rangle]|^2}}. \tag{33}$$

Once again, we emphasize that sensitivity refers to the minimum detectable variation of the angular velocity. Therefore, the gyroscope is more sensitive when $\Delta\Omega^2$ is smaller. Mathematically, this definition states that the product $(\Delta\Omega^2)^2 \times |\partial_{\Omega^2}[\langle I(\omega)\rangle - \langle I(-\omega)\rangle]|^2$ is equal to the noise of the photon current $\bar{N}_I(\omega)$. Note that the noise also represents the fluctuation [cf. Eq. (9)], so that Eq. (33) physically means that the fluctuation $\bar{N}_I(\omega)$ as the minimum change of the output photon current functions as the reference for observing variations of angular velocity.

When the quantum input $a_{\rm in}$ is in the vacuum state, Eq. (33) can be approximated as follows at the frequency $\omega = \omega_b$:

$$\Delta\Omega_v^2(\omega_b) \approx \frac{\gamma_x\gamma_y/4+\Omega^2}{4\sqrt{N_{\rm in}}}\left(1+\frac{\gamma_x\gamma_y/4+\Omega^2}{C_o\gamma_x\gamma_y}\right). \tag{34}$$

Note that the sensitivity is proportional to the thermal decay rates, and thus it tends to zero as the thermal decay rates tend to zero. In other words, the system can distinguish the infinitesimal changes of angular velocity in this extreme case. Physically, this extreme case means that the output photon current is extremely sensitive to the change of the angular velocity when the system is only affected by the shot noise.

It is not hard to show that the sensitivity has a fundamental limit

$$\Delta\Omega_v^2(\omega_b) \geq \frac{\gamma_x\gamma_y/4+\Omega^2}{2\sqrt{N_{\rm in}}}, \tag{35}$$

where the equality holds if and only if $C_o = (\gamma_x\gamma_y/4 + \Omega^2)/(\gamma_x\gamma_y)$. Notably, the condition $C_o \to \infty$ indicates that the coupling coefficient $g$ tends to infinity, which is impossible in realistic scenarios. This limitation reduces to the lowest bound of the sensitivity permitted by the standard quantum limit when $\Omega = 0$.

When the quantum input $a_{\rm in}$ is in the squeezed vacuum state, we have

$$\Delta\Omega_s^2(\omega_b) \approx e^{-r}\frac{\gamma_x\gamma_y/4+\Omega^2}{4\sqrt{N_{\rm in}}C_o\gamma_x\gamma_y}\sqrt{\left(\frac{\gamma_x\gamma_y}{4}+\Omega^2+e^{2r}C_o\gamma_x\gamma_y\right)^2+(1-e^{4r})C_o^2\gamma_x^2\gamma_y^2}. \tag{36}$$

Also, it gives the limitation

$$\Delta\Omega_s^2(\omega_b) \geq \sqrt{2(1+e^{-2r})}\frac{(\gamma_x\gamma_y/4+\Omega^2)^{3/2}}{4\sqrt{N_{\rm in}C_o\gamma_x\gamma_y}}, \tag{37}$$

where the equality holds if and only if $C_o = (\gamma_x\gamma_y/4 + \Omega^2)/(\gamma_x\gamma_y)$. The most significant point is that the sensitivity can be improved by squeezing, but the improvement is limited:

$$\frac{\Delta\Omega_s^2(\omega_b)}{\Delta\Omega_v^2(\omega_b)} = \sqrt{e^{-2r}+\frac{2(1-e^{-2r})C_o\gamma_x\gamma_y(\gamma_x\gamma_y/4+\Omega^2)}{(\gamma_x\gamma_y/4+\Omega^2+C_o\gamma_x\gamma_y)^2}} \leq \frac{\sqrt{2}}{2}\sqrt{1+e^{-2r}}. \tag{38}$$

The inequality in the second line shows that squeezing is not a very effective method for improving sensitivity, as sensitivity can only be enhanced up to $\sqrt{2}/2$ even when the squeezed parameter $r$ approaches infinity.

## IV. NUMERICAL RESULTS AND FURTHER DISCUSSION

So far, we have obtained constraints of the cooperativity and upper bounds of the angular velocity at the frequency $\omega = \omega_b$. Based on these constraints, we now simulate the SNR and sensitivity for further discussion. To this end, we first need to determine the range of the angular velocity according to Eqs. (29) and (31). However, the range receives little attention as one of the most important parameters of gyroscopes in recent works [18,19,24–28,35].

Before discussing the range, we also need to limit the squeezed parameter $r$. At present, the highest accessible degree of squeezing is 15 dB ($15 = 10\ \log_{10}(e^{2r})$, corresponds to $r \approx 1.73$) in experiments [56], such that the condition $C_o \geq \frac{1}{12}$ is also valid for Eq. (32) when $r \in [0, 1.73]$.

The numerical simulation of the upper bound of the angular velocity $\Omega^2$ as a function of the squeezed parameter $r$ is shown in Fig. 2. Here, the subscript ub is an abbreviation for the upper bound of inequalities (29) and (31). The solid and dashed lines represent the cases of quantum fluctuation input $a_{\text{in}}$ in the squeezed vacuum state and the vacuum state, respectively. Moreover, cooperativity $C_o$ is limited in the vicinity of the impedance matching condition $C_o = 1$, which is widely utilized in experiments [55]. Also, we use the gridline with $r = 1.73$ to mark the highest achievable squeezed degree in experiments. The differences between the solid and dashed lines demonstrate that squeezing can enhance the upper bound of the angular velocity $\Omega^2$ by up to 2 times within the accessible range of the squeezed parameter $r$. Moreover, the upper bound of the angular velocity $\Omega^2$ increases monotonically with increasing cooperativity $C_o$, whether the quantum input $a_{\text{in}}$ is in the vacuum state or the squeezed vacuum state. Note that cooperativity $C_o$ represents the coupling strength between the quantity to be measured and the readout cavity, and thus maintaining a higher coupling strength in experiments can result in a larger range for the gyroscope.

Based on the upper bounds of the angular velocity $\Omega^2$ mentioned above, we simulate the SNR under different cooperativities $C_o$, as depicted in Fig. 3. We plot the case of the quantum fluctuation input $a_{\text{in}}$ in the vacuum state in Fig. 3(a), and the case of $a_{\text{in}}$ in the squeezed vacuum state in Figs. 3(b) and 3(c). Also, we use gridlines to mark the upper bounds of the angular velocity, and we use black dashed lines to label the critical readable condition $\text{SNR}(\omega_b) = 1$. From Figs. 3(a) and 3(b), one can see that the SNR per photon $\text{SNR}(\omega_b)/N_{\text{in}}$ monotonously increases with increasing cooperativity $C_o$, where we fixed the

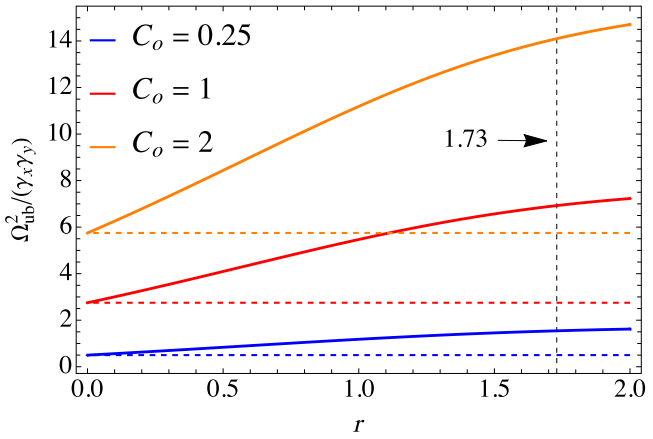


FIG. 2. Numerical simulations of the range $\Omega^2$ under different cooperativities $C_o$. The solid (dashed) lines represent the quantum input $a_{\text{in}}$ in the squeezed vacuum (vacuum) state, and the gridline is used to mark the accessible highest squeezed parameter $r = 1.73$ in experiments [56]. The differences between the solid and dashed lines demonstrate that squeezing is an effective way for expanding the upper bounds of the angular velocity $\Omega^2$. Also, the degree of the extent of this expansion increases as the squeezed parameter $r$ increases.

squeezed parameter $r = 1.73$ in Fig. 3(b). Therefore, maintaining a higher cooperativity $C_o$ can not only yield a wider range, but also improve readability. This result extends the findings presented in Fig. 2. One can also see that the SNR per photon monotonically decreases as the angular velocity increases. This result shows that readability improves when the angular velocity is reduced, especially when the quantum fluctuation input $a_{\text{in}}$ is squeezed. In Fig. 3(c), we replot the SNR per photon $\text{SNR}_s(\omega_b)/N_{\text{in}}$ as a function of the squeezed parameter $r$ under different cooperativities $C_o$, where we fixed the angular velocity $\Omega^2 = \gamma_x\gamma_y$. Under different cooperativities, all three curves of the SNR per photon monotonically increase with increasing squeezing parameter. Therefore, a higher degree of squeezing is beneficial for further improving the readability of the gyroscope.

Upon completing the discussions on the range and SNR per photon, we now shift our focus to the sensitivity, which is the most crucial index for gyroscopes. The corresponding numerical simulation is shown in Fig. 4. In Fig. 4(a), we use solid (dashed) lines to represent the case of the quantum fluctuation input $a_{\text{in}}$ in the squeezed vacuum (vacuum) state. We also use gridlines to mark the corresponding upper bounds of the angular velocity $\Omega^2_{\text{ub}}$ for a given cooperativity $C_o$. One can observe that $\sqrt{N_{\text{in}}}\Delta\Omega^2(\omega_b)$ decreases as the cooperativity $C_o$ increases. This implies that the system is capable of discerning smaller changes in angular velocity $\Omega^2$ when the cooperativity $C_o$ is higher. Furthermore, one can also see that $\sqrt{N_{\text{in}}}\Delta\Omega^2(\omega_b)$ monotonously increases with increasing

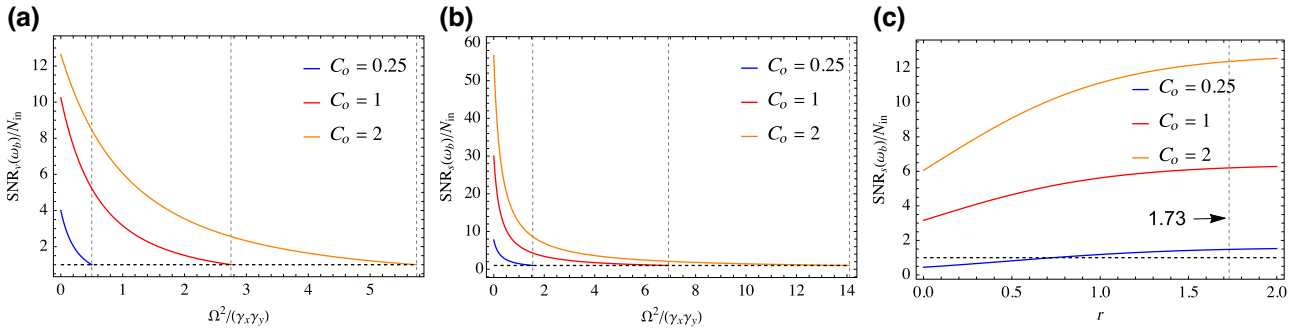


FIG. 3. Numerical simulations of the signal-to-noise ratio per photon $\mathrm{SNR}(\omega_b)/N_{\mathrm{in}}$ at various cooperativities $C_o$. The black dashed line represents the critical condition for readability $\mathrm{SNR}(\omega_b) = 1$. The gridlines are used to label the upper bounds of the angular velocity $\Omega^2_{\mathrm{ub}}$ in (a) and (b), and to label the accessible highest squeezed parameter $r$ in (c). (a) The quantum input $a_{\mathrm{in}}$ is in the vacuum state. (b) The quantum input $a_{\mathrm{in}}$ is in the squeezed vacuum state, where we have fixed the squeezed parameter $r = 1.73$. Comparing (a) with (b), one can see that the signal-to-noise ratio per photon is significantly improved under the same cooperativity $C_o$ after squeezing. (c) The SNR per photon $\mathrm{SNR}_s(\omega_b)/N_{\mathrm{in}}$ as a function of the squeezed parameter $r$ with a fixed $\Omega^2 = \gamma_x\gamma_y$. We observe that the blue solid line is not consistently higher than the black dashed line. Therefore, the squeezed parameter $r$ cannot be too small to ensure readability when the cooperativity $C_o = 0.25$.

angular velocity $\Omega^2$. This indicates that our gyroscope is more sensitive to smaller angular velocities. In Fig. 4(b), we replot the sensitivity $\sqrt{N_{\mathrm{in}}}\Delta\Omega^2_s(\omega_b)$ as a function of the squeezed parameter $r$ with fixed angular velocity $\Omega^2 = 0$. Here, we also use gridlines to mark the highest accessible squeezed parameter $r = 1.73$, and we use a black dashed line to label the standard quantum limit obtained from Eq. (35). In addition, we appropriately extend the squeezed parameter $r$ to observe limitation (37). We observe that the sensitivity $\sqrt{N_{\mathrm{in}}}\Delta\Omega^2_s(\omega_b)$ is consistently lower than the standard quantum limit when the quantum fluctuation input $a_{\mathrm{in}}$ is squeezed. Moreover, $\sqrt{N_{\mathrm{in}}}\Delta\Omega^2_s(\omega_b)$ decreases monotonically with increasing squeezed parameter $r$ and eventually approaches its limit. Again, this result shows that using a squeezed vacuum state reduces $\sqrt{N_{\mathrm{in}}}\Delta\Omega^2_s(\omega_b)$, but it is not the most effective method. Also, $\sqrt{N_{\mathrm{in}}}\Delta\Omega^2_s(\omega_b)$ decreases as the cooperativity $C_o$ increases. Therefore, maintaining higher cooperativity $C_o$ in experiments is beneficial for improving sensitivity. For the sake of clear comparisons, we plot the ratio $\Delta\Omega^2_s(\omega_b)/\Delta\Omega^2_v(\omega_b)$ as a function of the squeezed parameter $r$ in Fig. 4(c). In this plot, we set the angular velocity $\Omega = 0$. Here, the solid lines are plotted based on equality, while the black dashed line is plotted based on the inequality in Eq. (38). Obviously, the ratio $\Delta\Omega^2_s(\omega_b)/\Delta\Omega^2_v(\omega_b)$ is always lower than $\sqrt{2}/2$. Therefore, $\sqrt{N_{\mathrm{in}}}\Delta\Omega^2_s(\omega_b)$ can only be reduced by a maximum of $\sqrt{2}/2$.

We end this section by providing a brief review of our numerical simulations. Firstly, maintaining higher cooperativity $C_o$ in experiments is beneficial for obtaining a wider range, a higher SNR per photon, and a higher sensitivity. Secondly, using a squeezed vacuum state as the input reduces the minimum detectable change of the angular velocity, but it decreases by a maximum of $\sqrt{2}/2$.

## V. DISCUSSIONS ON EXPERIMENTS

As a theoretical proposal, our ultimate aim is to guide experiments. In this section, we focus on the following issues that may be of concern in experiments: the calibration of the output signal and the effects induced by nonzero detuning.

### A. Calibration of the output signal

In this work, the measurement depends on the spectral height of the output signal. This requires us to calibrate the spectral height before use, as actual measurements may introduce unavoidable deviations that would render the measured data inaccurate. Here, we briefly demonstrate how to calibrate the signal utilizing Eqs. (25) and (29). One can also use a similar approach to establish another calibration based on Eqs. (25) and (31) when the input is in the squeezed vacuum state.

According to Eqs. (25) and (29), an approximate spectral height can be acquired at $\Omega = 0$ and $\Omega^2 = (3C_o - \frac{1}{4})\gamma_x\gamma_y$ as

$$S(\omega_b) \approx \begin{cases} 256N_{\mathrm{in}}C_o^2, & \Omega = 0, \\ \frac{16}{9}N_{\mathrm{in}}, & \Omega^2 = (3C_o - \frac{1}{4})\gamma_x\gamma_y, \end{cases} \tag{39}$$

which is used in the following calibration. The angular velocity $\Omega^2$ can be readout from the spectral height $S(\omega_b)$ using the inverse function of Eq. (25):

$$\left(\frac{\gamma_x\gamma_y}{4} + \Omega_r^2\right)^2 = \frac{16N_{\mathrm{in}}C_o^2\gamma_x^2\gamma_y^2}{S_r(\omega_b)} \tag{40}$$

with subscript $r$ labeling the real value. Using the above equation and the spectral heights (39), one can plot

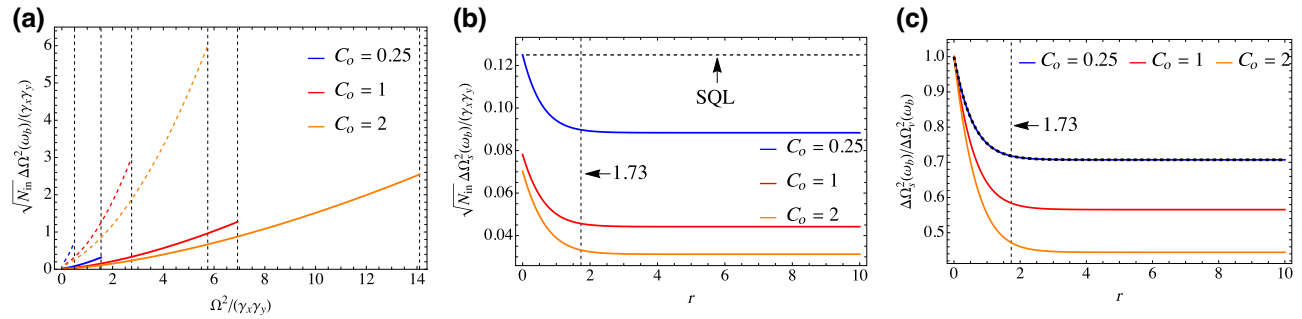


FIG. 4. The numerical simulation of the sensitivity $\sqrt{N_{\rm in}}\Delta\Omega^2(\omega_b)$. In (a), the solid (dashed) lines represent the case of the quantum fluctuation input $a_{\rm in}$ in the squeezed vacuum (vacuum) state. Gridlines are used to label the corresponding upper bounds of the angular velocity $\Omega^2_{\rm ub}$. Also, we set the squeezed parameter $r = 1.73$ when plotting the solid lines. Under the same cooperativity $C_o$, one can observe that $\sqrt{N_{\rm in}}\Delta\Omega^2(\omega_b)$ decreases significantly after squeezing. In (b), we plot $\sqrt{N_{\rm in}}\Delta\Omega^2(\omega_b)$ as a function of the squeezed parameter $r$ with fixed angular velocity $\Omega = 0$ in solid lines. The black dashed line marks the standard quantum limit obtained from Eq. (35). One can see that all three solid lines are lower than the black dashed line, indicating that squeezing is an effective method for surpassing the standard quantum limit. In addition, $\sqrt{N_{\rm in}}\Delta\Omega_s^2(\omega_b)$ decreases as the squeezed parameter $r$ increases and eventually approaches its limitation (37). This indicates that squeezing is not an effective method for further improving the sensitivity. In (c), for the sake of clear comparison with the case of the quantum fluctuation input $a_{\rm in}$ in the vacuum state, we replot the ratio $\Delta\Omega_s^2(\omega_b)/\Delta\Omega_v^2(\omega_b)$ as a function of the squeezed parameter $r$ with fixed angular velocity $\Omega = 0$. Here, the black dashed line is plotted based on the inequality of Eq. (38). We can clearly see that the sensitivity can only be improved by up to $\sqrt{2}/2$ after squeezing.

$(\gamma_x\gamma_y/4 + \Omega_r^2)^2$ as a function of the spectral height $S_r(\omega_b)$ as the reference curve.

Although the angular velocity $\Omega$ can be theoretically readout from the reference curve, there may be some deviations caused by the measuring instruments or other factors. Therefore, the sensor needs to be calibrated before use. In experiments, It is common practice to use multiple key points within the range to calibrate a sensor. For instance, one can obtain a spectral height $S_{m,1}(\omega_b)$ at a given measured angular velocity $\Omega_{m,1}$ and obtain another spectral height $S_{m,2}(\omega_b)$ at another measured angular velocity $\Omega_{m,2}$, and so on. With these measurement values, one can construct a measured curve that satisfies the equation

$$\left(\frac{\gamma_x\gamma_y}{4} + \Omega_m^2\right)^2 = \frac{16N_{\rm in}C_o^2\gamma_x^2\gamma_y^2}{S_m(\omega_b)}. \tag{41}$$

However, as discussed, the measured spectral height $S_m(\omega_b)$ would deviate from the real ones, i.e., $S_m(\omega_b) = S_r(\omega_b) \pm \delta S(\omega_b)$, where $\delta S(\omega_b) > 0$ is a slight shift caused by the measuring. Based on the real curve plotted as Eq. (40), we can choose $\Omega_r = 0$ and $\Omega_r^2 = (3C_o - \frac{1}{4})\gamma_x\gamma_y$ to calibrate the measured curve (41). The detailed calibration should consider the following two situations encountered in experiments.

(i) The measurement only leads to a shift $\delta S(\omega_b)$ in the spectral height, but does not affect the angular velocity $\Omega$. Therefore, the measured angular velocity $\Omega_m$ equals the real value $\Omega_r$ in this case. Notably, both curves (40) and (41) monotonically decrease as the spectral height increases. Therefore, these two curves do not intersect in this case. One can use the difference between the measured height $S_m(\omega_b)$ and the theoretical real height $S_r(\omega_b)$ at $\Omega = 0$ or $\Omega^2 = (3C_o - \frac{1}{4})\gamma_x\gamma_y$ to calculate the shift $\delta S(\omega_b)$.

(ii) The shift in the spectral height $\delta S(\omega_b)$ also results in a modification of the angular velocity $\delta\Omega_r^2 > 0$, causing $\Omega_m^2 = \Omega_r^2 \pm \delta\Omega_r^2$, and $\delta\Omega_r^2$ is possibly not fixed. In this case, Eq. (41) is rewritten as

$$\left(\frac{\gamma_x\gamma_y}{4} + \Omega_r^2 \mp \delta\Omega_r^2\right)^2 = \frac{16N_{\rm in}C_o^2\gamma_x^2\gamma_y^2}{S_r(\omega_b) \pm \delta S(\omega_b)}, \tag{42}$$

when the measured signal $S_m(\omega)$ is less than the real signal $S_r(\omega)$, i.e., $\delta S(\omega)$ takes the minus sign, the modification $\delta\Omega_r$ takes the positive sign. In the versa case, $\delta\Omega_r$ takes the minus sign and $\delta S(\omega)$ takes the positive sign. This is because $S_m(\omega_b) \propto (1/\Omega_m^2)$ is a square inverse function, see Eq. (41). We can then establish a relationship between $\delta S(\omega_b)$ and $\delta\Omega_r^2$ by dividing Eq. (42) by Eq. (40) on both sides, i.e.,

$$\left(1 \mp \frac{\delta\Omega_r^2}{\gamma_x\gamma_y/4 + \Omega_r^2}\right)^2 = \frac{S_r(\omega_b)}{S_r(\omega_b) \pm \delta S(\omega_b)}, \tag{43}$$

and further obtain a correction relation

$$\frac{1}{[1 \mp \delta\Omega_r^2/(\gamma_x\gamma_y/4 + \Omega_r^2)]^2} - 1 = \pm\frac{\delta S(\omega_b)}{S_r(\omega_b)}. \tag{44}$$

Notably, the real curve (40) and the measured curve (41) would intersect in this case. Therefore, $\delta\Omega_r^2$ as a function of $\delta S(\omega_b)$ has two points that can be used as references.

The first point occurs at $\Omega_r = 0$ with $S_r(\omega_b) \approx 256 N_{\rm in} C_o^2$ and $\delta S(\omega_b)$ is obtained from the data $S_m(\omega_b)$, allowing one to extract the modification $\delta\Omega_r^2|_{\Omega_r=0}$. The second point occurs at the intersection. At this point, the shift $\delta S(\omega_b) = 0$ implies that $\delta\Omega_r^2|_{\Omega_r^2=\text{intersection}} = 0$, and the real angular velocity $\Omega_r$ can be directly extracted from the theoretical real curve $S_r(\omega_b)$. Based on these two points and Eq. (44), one can plot a correction curve $\delta\Omega_r^2$ as a function of $\delta S(\omega_b)$ to calibrate the measured signal. If one wants to calibrate the signal more accurately, one can expand Eq. (44) as a Taylor series and keep it to the desired order:

$$
\begin{aligned}
+\frac{\delta S(\omega_b)}{S_r(\omega_b)} &= \frac{1}{[1-\delta\Omega_r^2/(\gamma_x\gamma_y/4+\Omega_r^2)]^2} - 1 = \left[\sum_{n=0}^{\infty}\left(\frac{\delta\Omega_r^2}{\gamma_x\gamma_y/4+\Omega_r^2}\right)^n\right]^2 - 1 \\
&= \left(1 + \frac{\delta\Omega_r^2}{\gamma_x\gamma_y/4+\Omega_r^2} + \text{higher-order terms}\right)^2 - 1, \\
-\frac{\delta S(\omega_b)}{S_r(\omega_b)} &= \frac{1}{[1+\delta\Omega_r^2/(\gamma_x\gamma_y/4+\Omega_r^2)]^2} - 1 = \left[\sum_{n=0}^{\infty}(-1)^n\left(\frac{\delta\Omega_r^2}{\gamma_x\gamma_y/4+\Omega_r^2}\right)^n\right]^2 - 1 \\
&= \left(1 - \frac{\delta\Omega_r^2}{\gamma_x\gamma_y/4+\Omega_r^2} + \text{higher-order terms}\right)^2 - 1,
\end{aligned}
$$

In the above derivation, for convenience, we have exchanged both sides of the equal sign. If one does not require very high accuracy in realistic calibrations, one can keep the above equations to the first order and derive a linear correction relation $\delta S(\omega_b)/S_r(\omega_b) = 2\delta\Omega_r^2/(\gamma_x\gamma_y/4+\Omega_r^2)$ for a given $\Omega_r^2$.

In summary, the calibration of our gyroscope is based on the approximate expression (25), and our double-point calibration is a common method in experiments. In the specific calibration process, different calibration strategies need to be selected based on whether there is an intersection between the measured curve and the theoretical real curve.

### B. The effects induced by a nonzero detuning

In Secs. II–IV we employed two important assumptions: (i) the system is resonantly driven, i.e., $\Delta = 0$; (ii) the state of the readout cavity adiabatically tracks the motion of the $b_x$ mode. These assumptions simplify the susceptibility function of the readout cavity, as shown in Eq. (7). These two assumptions are too idealistic for experiments. Therefore, we provide a detailed discussion to demonstrate how a nonzero detuning $\Delta$ affects the system.

Here, we also assume that the frequency of the SAW cavity is much lower than the damping of the readout cavity, i.e., $\omega_b \ll \kappa$. So, the readout cavity rapidly evolves to its steady state compared to the SAW cavity, resulting in the susceptibility function

$$\chi_a = \frac{1}{i\Delta - \kappa/2}, \tag{45}$$

and the modified detuning

$$\tilde{\Delta} = \frac{\gamma_x C_o}{2}\frac{\Delta\kappa}{\Delta^2+\kappa^2/4}. \tag{46}$$

With the above two equations, we further rewrite the output noise (14) and the signal (24) as

$$
\begin{aligned}
\bar{N}_I(\omega) &= 1 + \frac{\gamma_x C_o}{4}\frac{\kappa^4}{(\Delta^2+\kappa^2/4)^2} \\
&\quad\times\left[\bar{N}_X(\omega) - \frac{i\Delta}{\kappa}[Q_1(\omega) - Q_1^*(\omega)]\right], \qquad (47) \\
S(\omega) &= \frac{N_{\rm in}\gamma_x^2 C_o^2}{16}\frac{\kappa^6(\kappa\sin\varphi - 2\Delta\cos\varphi)^2}{(\Delta^2+\kappa^2/4)^4} \\
&\quad\times|Q_1(\omega) - Q_1(-\omega)|^2 \qquad (48)
\end{aligned}
$$

with

$$Q_1(\omega) = \frac{\chi_x(\omega) - \chi_x^*(-\omega)}{1 + i\tilde{\Delta}[\chi_x(\omega) - \chi_x^*(-\omega)]}, \tag{49a}$$

$$\bar{N}_X(\omega) = \sum_{i=1}^{3}\frac{1}{2}[|P_i(\omega)|^2 + |P_i(-\omega)|^2]. \tag{49b}$$

If we set $\varphi = \pi/2$ and let $\Delta = 0$, Eqs. (48) and (47) then reduce to Eqs. (24) and (14), respectively.

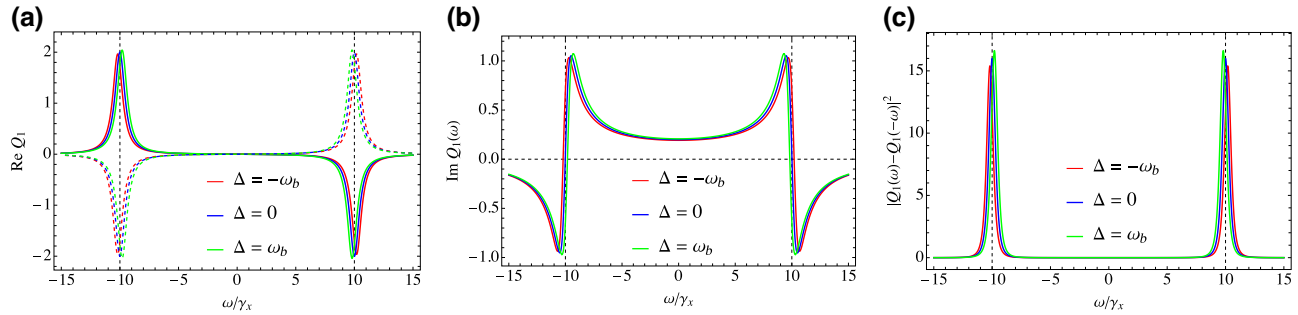


FIG. 5. Numerical simulations of the susceptibility function $Q_1(\omega)$ under different detunings $\Delta$. Here, the parameters $\gamma_x = \gamma_y = 1, \omega_b = 10\gamma_x, \kappa = 100\gamma_x, C_o = 1, \Omega = 0$ are used in plotting. Gridlines are employed to mark the centers of the peaks at $\omega = \pm\omega_b$. (a) The real parts of $Q_1(\omega)$ (solid lines) and $Q_1(-\omega)$ (dashed lines) represent the emission and absorption of the $b_x$ mode to the inputs, respectively. The nonzero detuning $\Delta$ slightly shifts the original centers of the peaks from $\omega = \pm\omega_b$ to $\omega = \pm\omega_b \pm 2C_o\gamma_x\Delta/\kappa$. Besides, the symmetry between $\mathrm{Re}\,Q_1(\omega)$ and $\mathrm{Re}\,Q_1(-\omega)$ indicates that the system is energy conserved. (b) The imaginary part of $\mathrm{Im}\,Q_1(\omega)$ represents the dispersion relation of the intracavity field. The slow/fast-light dividing line $\mathrm{Im}\,Q_1(\omega) = 0$ also changes as the detuning $\Delta$ changes, similar to the peaks' centers in (a). (c) Plot of $|Q_1(\omega) - Q_1(-\omega)|^2$ under different detunings $\Delta$. Notably, the peak values of the red and green lines differ because the effective parts $\mathrm{Im}\{[\chi_x(\omega) - \chi_x^*(-\omega)]^{-1}\} + \tilde{\Delta}$ are not the same when the detuning $\Delta$ takes an opposite sign.

To fully discuss the influences induced by the nonzero detuning, we first check the susceptibility function $Q_1(\omega)$ and its negative-frequency part $Q_1(-\omega)$. Notably, $Q_1(\omega)$ [also $Q_1(-\omega)$] is a double-peak Lorentz lineshape with real part $\mathrm{Re}\{[\chi_x(\omega) - \chi_x^*(-\omega)]^{-1}\}$ and effective imaginary part $\mathrm{Im}\{[\chi_x(\omega) - \chi_x^*(-\omega)]^{-1}\} + \tilde{\Delta}$, and these double peaks occur at $\omega = \pm\omega_b$ when $\Delta = 0$. Therefore, the nonzero detuning induces a slight modification $\tilde{\Delta}$ on the centers of the peaks. Note that the modification $\tilde{\Delta}$ is proportional to a Lorentzian coefficient $\Delta\kappa/(\Delta^2 + \kappa^2/4)$, such that it reaches the maximum at $\Delta = \pm\kappa/2$, and the modification direction depends on the sign of the detuning $\Delta$. In our proposal, we consider that the condition $\gamma_{x,y} < \omega_b \ll \kappa$ holds. If the detuning $\Delta$ is much smaller than the linewidth of the readout cavity $\kappa$, the modification $\tilde{\Delta} \simeq 2C_o\gamma_x\Delta/\kappa$ can be regarded as a second-order small quantity, playing a negligible role.

In Fig. 5, we provide a numerical simulation of $Q_1(\omega)$ within the range of $\Delta = \pm\omega_b$. When the detuning $\Delta$ is much smaller than the linewidth of the readout cavity, it is evident that all three curves almost overlap in each subfigure. Therefore, we use gridlines to label only the original centers $\omega = \pm\omega_b$. In Fig. 5(a), we plot the $\mathrm{Re}\,Q_1(\omega)$ [$\mathrm{Re}\,Q_1(-\omega)$] with solid lines (dashed lines),

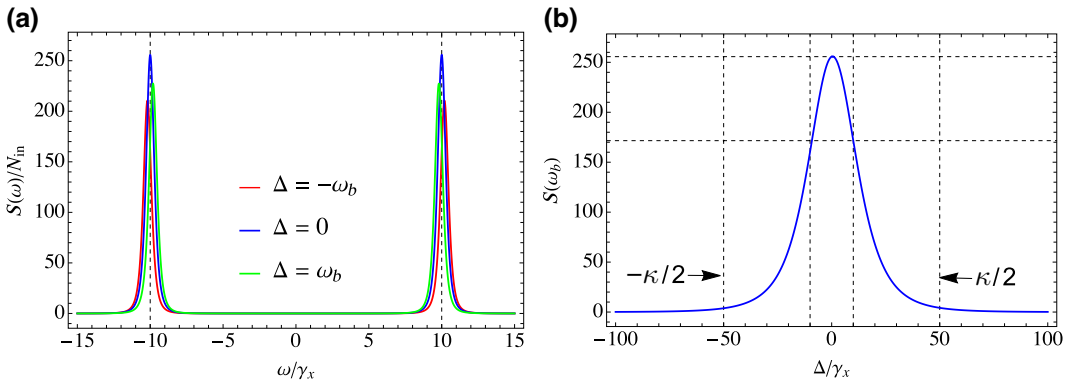


FIG. 6. Numerical simulations of output signal $S(\omega)$ under different detunings $\Delta$. Here, the parameters $\gamma_x = \gamma_y = 1, \omega_b = 10\gamma_x, \kappa = 100\gamma_x, C_o = 1, \Omega = 0, \varphi = \pi/2$ are used in plotting. (a) The output signal $S(\omega)$ is a function of $\omega$. Gridlines are also used to mark the centers of the peaks at $\omega = \pm\omega_b$. Because of the Lorentzian filtering effect of the readout cavity, the peak values decrease when the detuning $\Delta$ shifts from the center. (b) The peak value $S(\omega_b)$ as a function of the detuning $\Delta$. We add another set of gridlines to mark the linewidth of the readout cavity $[-\kappa/2, \kappa/2]$. The nonzero detuning causes the readout cavity to function as a filter, shaping the output signal into a strict Lorentz lineshape across the detuning $\Delta$. Also, we observe that $S(\omega_b)|_{\Delta=0} \approx 0.67S(\omega_b)|_{\Delta=\omega_b}$ from the gridlines on the $y$ axis. This indicates that the filtering effect could visibly decrease the peak value of the output signal $S(\omega_b)$, even when the detuning $\Delta$ is significantly smaller than the linewidth of the readout cavity $\kappa$.

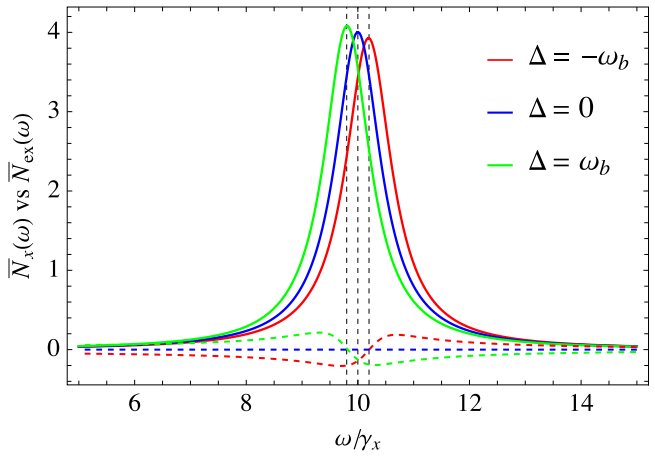


FIG. 7. Numerical simulations of noises $\bar{N}_x(\omega)$ (solid lines) and $\bar{N}_{ex}(\omega)$ (dashed lines) under different detunings $\Delta$. Here, the parameters $\gamma_x = \gamma_y = 1, \omega_b = 10\gamma_x, \kappa = 100\gamma_x, C_o = 1, \Omega = 0$ are used in plotting. Gridlines are used to label the centers of the peaks: $\omega_b - \gamma_x/2 - 2C_o\gamma_x\Delta/\kappa$, $\omega_b$, and $\omega_b + \gamma_x/2 - 2C_o\gamma_x\Delta/\kappa$ (from left to right). In the regime $\omega \in [\omega_b - 2C_o\gamma_x\Delta/\kappa, \omega_b + 2C_o\gamma_x\Delta/\kappa]$, the extra noise takes a negative sign, such that a nonzero detuning $\Delta$ results in an inhibitory effect on the total noise $\bar{N}_I(\omega)$.

which represent the emission (absorption) of the $b_x$ mode to the inputs. One can observe that the nonzero detuning $\Delta$ slightly changes the original centers of the peaks from $\omega = \pm\omega_b$ to $\omega = \pm\omega_b \pm 2C_o\gamma_x\Delta/\kappa$. Besides, $\mathrm{Re}\,Q_1(\omega)$ and $\mathrm{Re}\,Q_1(-\omega)$ are symmetric over the $y$ axis, indicating that the system is energy conserved. In Fig. 5(b), we only plot $\mathrm{Im}\,Q_1(\omega)$ representing the dispersion relation of the intracavity field, as $\mathrm{Im}\,Q_1(-\omega)$ is completely overlapped to $\mathrm{Im}\,Q_1(\omega)$. Analogous to the peaks' centers in Fig. 5(a), the dividing line of fast and slow lights $\mathrm{Im}\,Q_1(\omega) = 0$ in Fig. 5(b) also changes as the detuning $\Delta$ changes. Also, the antisymmetric susceptibility function $|Q_1(\omega) - Q_1(-\omega)|^2$ is plotted in Fig. 5(c). It should be noted that the peak values of the red and green lines differ as the detuning $\Delta$ changes sign since the effective imaginary parts $\mathrm{Im}\{[\chi_x(\omega) - \chi_x^*(-\omega)]^{-1}\} + \tilde{\Delta}$ $\tilde{\Delta}$ are not the same when the detuning $\Delta$ takes on an opposite sign.

After discussing the susceptibility function $Q_1(\omega)$, we now shift our focus to the output signal (48). The nonzero detuning also introduces a Lorentzian coefficient $\kappa^6(\kappa\sin\varphi - 2\Delta\cos\varphi)^2/(\Delta^2 + \kappa^2/4)^4$, which implies that the readout cavity acts as a filter and shapes the output signal to a Lorentzian lineshape. Here, we provide the corresponding numerical simulation in Fig. 6 using the same parameters and setting the phase $\varphi = \pi/2$. In Fig. 6(a), the gridlines also label the original centers of the peaks at $\omega = \pm\omega_b$. Analogous to the results in Fig. 5(c), the nonzero detuning also shifts the centers of the peaks of the output signal. Besides, the nonzero detuning $\Delta$ also causes the readout cavity to function as a filter, shaping the spectra into strict Lorentz lineshapes, but with varying peak values. To demonstrate the changes in the peak value $S(\omega_b)$ as a function of the detuning $\Delta$, we plot it in Fig. 6(b), where we include an additional set of gridlines to indicate the linewidth of the readout cavity $[-\kappa/2, \kappa/2]$. Because of the filtering effect caused by the readout cavity, the peak value also exhibits a strict Lorentzian lineshape across the detuning $\Delta$. Besides, from the two gridlines on the $y$ axis, we can clearly see that $S(\omega_b)|_{\Delta=\omega_b} \approx 0.67S(\omega_b)|_{\Delta=0}$. Therefore, although the detuning $\Delta$ is much smaller than the linewidth of the readout cavity, the resulting filtering effect induces an apparent reduction in the peak value of the output signal $S(\omega)$.

As for the noise (47), the nonzero detuning leads to an extra noise $\bar{N}_{ex}(\omega) = -i\Delta[Q_1(\omega) - Q_1^*(\omega)]/\kappa$. To demonstrate the extent of this extra noise, we plot $\bar{N}_x(\omega)$ and $\bar{N}_{ex}(\omega)$ as a function of $\omega$ in Fig. 7. Here, $\bar{N}_x(\omega)$ and $\bar{N}_{ex}(\omega)$ are plotted with solid and dashed lines, respectively. Notably, the nonzero noise $\bar{N}_x(\omega)$ only appears in the vicinity of $\omega_b$, so we only plot $\bar{N}_x(\omega_b)$. The regime worth noting is $\omega \in [\omega_b - 2C_o\gamma_x\Delta/\kappa, \omega_b + 2C_o\gamma_x\Delta/\kappa]$, which is marked by the gridlines from left to right. In this regime, the extra noise $\bar{N}_{ex}(\omega)$ is negatively signed, indicating that a nonzero detuning leads to a slightly inhibitory impact on the total noise $\bar{N}_I(\omega_b)$.

## VI. CONCLUSION

In conclusion, we have proposed a quantum gyroscope that utilizes a coupled cavity system. We start by discussing the noise power spectral density under resonant driving and delve into the details of the standard quantum limit. We systematically analyze all three crucial indices for gyroscopes (range, signal-to-noise ratio, and sensitivity), instead of focusing on just one of them, as done in recent proposals [18,19,24–28]. Based on this comprehensive analysis, we provide fundamental sensitivity limits for quantum inputs in the vacuum and squeezed vacuum states, respectively. However, the two fundamental limits of sensitivity are the most important index of gyroscopes, yet they have received little attention in the aforementioned proposals, particularly when the quantum input is squeezed. More importantly, we find that squeezing can enhance sensitivity and surpass the standard quantum limit. However, this enhancement can only reach up to $\sqrt{2}/2$ even as the squeezing parameter approaches infinity. This result provides a basis for guiding experiments, indicating that squeezing is not a very effective method for further improving sensitivity.

We have also provided a detailed discussion on the nonresonant driving case. The nonzero detuning only induces a slight modification $\tilde{\Delta}$ on the imaginary part of the susceptibility function of the $x$ mode, thus shifting the centers of the Lorentzian peaks from $\omega = \pm\omega_b$ to $\omega = \pm\omega_b \pm \tilde{\Delta}$. Also, the nonzero detuning causes the readout cavity to

function as a Lorentz filter, and thus it shapes the output signal to a strict Lorentz lineshape across the detuning. In addition, the nonzero detuning introduces an extra component to the noise of the photon current. This extra noise could exhibit a slightly inhibitory effect on the noise of the photon current within the interval $\omega_b \in [\omega_b - \tilde{\Delta}, \omega_b + \tilde{\Delta}]$.

As a theoretical proposal, we focus not only on designing gyroscopes, but also on fully demonstrating the calibration of the output signal through a double-point calibration method. We further provide an analytical correction relation between the spectral shift induced by the measurements $\delta S(\omega_b)$ and the resulting modification of the angular velocity $\delta\Omega_r^2$. Therefore, our proposal provides valuable guidance for experiments.

## ACKNOWLEDGMENTS

This work is supported by the National Natural Science Foundation of China (NSFC) under Grants No. 62273226 and No. 61873162.

## APPENDIX: HAMILTONIAN OF THE DOUBLE-MODE OSCILLATOR IN A ROTATING PLATFORM

In this appendix we start by introducing the Lagrangian and then proceed to derive the Hamiltonian of a double-mode mechanical oscillator in a rotating coordinate system. According to the model in Fig. 1, the coordinate systems before and after rotation are shown in Fig. 8. The $x_o$-$y_o$ coordinate system (inertial system, plotted in black) rotates counterclockwise with an angular velocity $\Omega$ and then transforms into the $x$-$y$ coordinate system (noninertial system, plotted in red). After time $t$, the rotated angle is $\theta = \int_0^t \mathrm{d}\tau\, \Omega$. In doing so, the positions of the mechanical oscillator (shadow box) in the two systems are $(x_o, y_o)$ and $(x, y)$, respectively. The transformation relation between

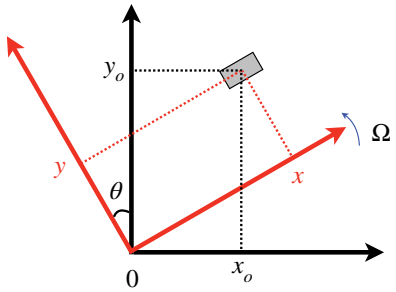


FIG. 8. Schematic of coordinate systems before and after rotation, where the shaded box represents the double-mode oscillator. The $x_o$-0-$y_o$ coordinate system (inertial system, plotted in black) rotates counterclockwise with an angular velocity $\Omega$. After time $t$, it forms the $x$-0-$y$ coordinate system (noninertial system, plotted in red) such that the rotated angle is $\theta = \int_0^t \mathrm{d}\tau\, \Omega$.

coordinates in these two systems reads

$$\begin{pmatrix} x \\ y \end{pmatrix} = \begin{pmatrix} \cos\theta(t) & \sin\theta(t) \\ -\sin\theta(t) & \cos\theta(t) \end{pmatrix} \begin{pmatrix} x_o \\ y_o \end{pmatrix}. \tag{A1}$$

Correspondingly, the Lagrangian of the oscillator in the original system reads

$$\mathcal{L}_o = T_o - V_o \tag{A2}$$

with kinetic energy

$$T_o(\dot{x}_o, \dot{y}_o) = \frac{m}{2}(\dot{x}_o^2 + \dot{y}_o^2)$$

and potential energy

$$\begin{aligned} V_o(x_o, y_o) &= \tfrac{1}{2}[k_x(x - x_e)^2 + k_y(y - y_e)^2] \\ &= \frac{k_x}{2}[(x_o - x_{oe})\cos\theta(t) + (y_o - y_{oe})\sin\theta(t)]^2 \\ &\quad + \frac{k_y}{2}[-(x_o - x_{oe})\sin\theta(t) + (y_o - y_{oe}) \\ &\quad \times \cos\theta(t)]^2, \end{aligned}$$

where $k_{x(y)}$ is the spring constant of the $x(y)$ mode. Here, $x_e, y_e$ and $x_{oe}, y_{oe}$ are the equilibrium positions in the rotation system, while $x_{oe}$ and $y_{oe}$ represent the equilibrium positions in the original system. Lagrangian (A2) further gives the Hamiltonian

$$\begin{aligned} H_o(x_o, y_o, p_{o,x}, p_{o,y}) &= \frac{1}{2m}(p_{o,x}^2 + p_{o,y}^2) \\ &\quad + \frac{k_x}{2}[(x_o - x_{oe})\cos\theta(t) \\ &\quad + (y_o - y_{oe})\sin\theta(t)]^2 \\ &\quad + \frac{k_y}{2}[-(x_o - x_{oe})\sin\theta(t) \\ &\quad + (y_o - y_{oe})\cos\theta(t)]^2, \end{aligned} \tag{A3}$$

where the momenta $p_{x,o}, p_{y,o}$ conjugate to coordinates $x_o, y_o$ read

$$p_{x,o} = \frac{\partial \mathcal{L}_o}{\partial \dot{x}_o} = m\dot{x}_o, \tag{A4}$$

$$p_{y,o} = \frac{\partial \mathcal{L}}{\partial \dot{y}_o} = m\dot{y}_o. \tag{A5}$$

In addition, these two sets of conjugate operators satisfy the basic commutation relation $[x_o, p_{x,o}] = [y_o, p_{y,o}] = i\hbar$.

In the rotating system, the Lagrangian of the mechanical oscillator reads

$$\begin{aligned}\mathcal{L} &= T(\dot{x},\dot{y}) - V(x,y)\\ &= \frac{m}{2}(\dot{x}^2+\dot{y}^2) - \tfrac{1}{2}[k_x(x-x_o)^2 + k_y(y-y_o)^2]\\ &\quad + m\Omega(-\dot{x}y + x\dot{y}) + \frac{m\Omega^2}{2}(x^2+y^2),\end{aligned} \tag{A6}$$

where the first term on the right-hand side represents the translational kinetic energy, the second term is the potential energy, the third term denotes the energy induced by Coriolis forces, and the last term is the energy induced by the centrifugal forces. The last two terms are fictitious energies that arise from noninertial forces.

Similarly, Lagrangian (A6) gives the Hamiltonian

$$\begin{aligned}H(x,y,p_x,p_y) &= \frac{1}{2m}[(p_x + m\Omega y)^2 + (p_y - m\Omega x)^2]\\ &\quad + \tfrac{1}{2}[k_x(x-x_o)^2 + k_y(y-y_o)^2]\\ &\quad - \frac{m\Omega^2}{2}(x^2+y^2),\end{aligned} \tag{A7}$$

where the momenta $p_x, p_y$ conjugate to the coordinates $x, y$ are given by

$$p_x = \frac{\partial \mathcal{L}}{\partial \dot{x}} = m\dot{x} - m\Omega y, \tag{A8a}$$

$$p_y = \frac{\partial \mathcal{L}}{\partial \dot{y}} = m\dot{y} + m\Omega x. \tag{A8b}$$

The first term on the right-hand side of Eq. (A7) is the kinetic energy in the noninertial system, the second term denotes the potential energy, and the third term represents the energy induced by centrifugal forces. In Ref. [27], the authors do not take into account the influence of centrifugal forces, although the magnitude of the centrifugal forces can be much greater than that of the Coriolis forces. This approximation is valid only when considering the frequency $\omega = \omega_b$ instead of $\omega = 0$ in the power spectral density since the centrifugal forces only affect the zero-frequency component.

Furthermore, using Eqs. (A8a) and (A8b) and the relation

$$\begin{aligned}\begin{pmatrix}\dot{x}\\ \dot{y}\end{pmatrix} &= \Omega\begin{pmatrix}-\sin\theta(t) & \cos\theta(t)\\ -\cos\theta(t) & -\sin\theta(t)\end{pmatrix}\begin{pmatrix}x_o\\ y_o\end{pmatrix}\\ &\quad + \begin{pmatrix}\cos\theta(t) & \sin\theta(t)\\ -\sin\theta(t) & \cos\theta(t)\end{pmatrix}\begin{pmatrix}\dot{x}_o\\ \dot{y}_o\end{pmatrix},\end{aligned} \tag{A9}$$

one can easily check that the conjugate operators $x(y)$, $p_{x(y)}$ also satisfy the basic commutation relation $[x,p_x] = [y,p_y] = i\hbar$. In addition, Hamiltonian (A7) can be examined by deriving its classical equations of motion using the Hamilton canonical equation, which has the same form as the equations of motion derived from the Heisenberg equation.

Hamiltonian (A7) can be rewritten as Eq. (2a) in terms of creation and annihilation operators with the transformations

$$x = \sqrt{\frac{\hbar}{2m\omega_x}}(b_x + b_x^\dagger), \qquad p_x = -i\sqrt{\frac{m\hbar\omega_x}{2}}(b_x - b_x^\dagger),$$

$$y = \sqrt{\frac{\hbar}{2m\omega_y}}(b_y + b_y^\dagger), \qquad p_y = -i\sqrt{\frac{m\hbar\omega_y}{2}}(b_y - b_y^\dagger),$$

where the mechanical frequency is $\omega_{x(y)} = \sqrt{k_{x(y)}/m}$, and we set the equilibrium positions $x_o = y_o = 0$ for brevity in deriving Eq. (2a).


[1] J. D. Barr, Inertial guidance - *inertial guidance*. Charles Draper, Walter Wrigley and John Hovorka, J. Navig. **14,** 240 (1961).

[2] R. J. Craig, Theory of operation of an elastically supported tuned gyroscope, IEEE Trans. Aerosp. Electron. Syst. **AES-8**, 280 (1972).

[3] C. Acar and A. Shkel, *MEMS Vibratory: Structural Approaches to Improve Robustness Gyroscopes* (Springer New York, New York, 2008).

[4] M. N. Armenise, C. Ciminelli, F. Dell'Olio, and V. M. N. Passaro, *Advances in Gyroscope Technologies* (Springer Berlin, Heidelberg, 2010).

[5] W. W. Chow, J. Gea-Banacloche, L. M. Pedrotti, V. E. Sanders, W. Schleich, and M. O. Scully, The ring laser gyro, Rev. Mod. Phys. **57**, 61 (1985).

[6] F. Riehle, T. Kisters, A. Witte, J. Helmcke, and C. J. Bordé, Optical Ramsey spectroscopy in a rotating frame: Sagnac effect in a matter-wave interferometer, Phys. Rev. Lett. **67,** 177 (1991).

[7] T. L. Gustavson, P. Bouyer, and M. A. Kasevich, Precision rotation measurements with an atom interferometer gyroscope, Phys. Rev. Lett. **78**, 2046 (1997).

[8] J. P. Dowling, Correlated input-port, matter-wave interferometer: Quantum-noise limits to the atom-laser gyroscope, Phys. Rev. A **57**, 4736 (1998).

[9] T. L. Gustavson, A. Landragin, and M. A. Kasevich, Rotation sensing with a dual atom-interferometer Sagnac gyroscope, Class. Quantum Grav. **17**, 2385 (2000).

[10] D. S. Durfee, Y. K. Shaham, and M. A. Kasevich, Long-term stability of an area-reversible atom-interferometer Sagnac gyroscope, Phys. Rev. Lett. **97**, 240801 (2006).

[11] B. Canuel, F. Leduc, D. Holleville, A. Gauguet, J. Fils, A. Virdis, A. Clairon, N. Dimarcq, C. J. Bordé, A. Landragin, and P. Bouyer, Six-axis inertial sensor using cold-atom interferometry, Phys. Rev. Lett. **97**, 010402 (2006).

[12] J. K. Stockton, K. Takase, and M. A. Kasevich, Absolute geodetic rotation measurement using atom interferometry, Phys. Rev. Lett. **107**, 133001 (2011).
[13] P. Berg, S. Abend, G. Tackmann, C. Schubert, E. Giese, W. P. Schleich, F. A. Narducci, W. Ertmer, and E. M. Rasel, Composite-light-pulse technique for high-precision atom interferometry, Phys. Rev. Lett. **114**, 063002 (2015).
[14] I. Dutta, D. Savoie, B. Fang, B. Venon, C. L. Garrido Alzar, R. Geiger, and A. Landragin, Continuous cold-atom inertial sensor with 1 nrad/sec rotation stability, Phys. Rev. Lett. **116**, 183003 (2016).
[15] D. Savoie, M. Altorio, B. Fang, L. A. Sidorenkov, R. Geiger, and A. Landragin, Interleaved atom interferometry for high-sensitivity inertial measurements, Sci. Adv. **4**, eaau7948 (2018).
[16] Z.-W. Yao, H.-H. Chen, S.-B. Lu, R.-B. Li, Z.-X. Lu, X.-L. Chen, G.-H. Yu, M. Jiang, C. Sun, W.-T. Ni, J. Wang, and M.-S. Zhan, Self-alignment of a large-area dual-atom-interferometer gyroscope using parameter-decoupled phase-seeking calibrations, Phys. Rev. A **103**, 023319 (2021).
[17] E. R. Moan, R. A. Horne, T. Arpornthip, Z. Luo, A. J. Fallon, S. J. Berl, and C. A. Sackett, Quantum rotation sensing with dual Sagnac interferometers in an atom-optical waveguide, Phys. Rev. Lett. **124**, 120403 (2020).
[18] Y. Wu, J. Guo, X. Feng, L. Q. Chen, C.-H. Yuan, and W. Zhang, Atom-light hybrid quantum gyroscope, Phys. Rev. Appl. **14**, 064023 (2020).
[19] J. Guo, S. Ming, Y. Wu, L. Q. Chen, and W. Zhang, Super-sensitive rotation measurement with an orbital angular velocity atom-light hybrid interferometer, Opt. Express **29**, 208 (2021).
[20] K. F. Woodman, P. W. Franks, and M. D. Richards, The nuclear magnetic resonance gyroscope: A review, J. Navig. **40**, 366 (1987).
[21] T. W. Kornack, R. K. Ghosh, and M. V. Romalis, Nuclear spin gyroscope based on an atomic comagnetometer, Phys. Rev. Lett. **95**, 230801 (2005).
[22] D. Meyer and M. Larsen, Nuclear magnetic resonance gyro for inertial navigation, Gyroscopy Navig. **5**, 75 (2014).
[23] K. Zhang, N. Zhao, and Y.-H. Wang, Closed-loop nuclear magnetic resonance gyroscope based on Rb-Xe, Sci. Rep. **10**, 2258 (2020).
[24] S. Davuluri, Optomechanics for absolute rotation detection, Phys. Rev. A **94**, 013808 (2016).
[25] S. Davuluri, K. Li, and Y. Li, Gyroscope with two-dimensional optomechanical mirror, New J. Phys. **19**, 113004 (2017).
[26] K. Li, H. Fu, and Y. Li, Coriolis-force-induced coupling between two modes of a mechanical resonator for detection of angular velocity, Phys. Rev. A **98**, 023862 (2018).
[27] K. Li, S. Davuluri, and Y. Li, Three-mode optomechanical system for angular velocity detection, Chin. Phys. B **27**, 084203 (2018).
[28] K. Li, S. Davuluri, and Y. Li, Improving optomechanical gyroscopes by coherent quantum noise cancellation processing, Sci. China Phys. Mech. **61**, 90311 (2018).
[29] C. L. Degen, F. Reinhard, and P. Cappellaro, Quantum sensing, Rev. Mod. Phys. **89**, 035002 (2017).
[30] H.-K. Lau and A. A. Clerk, Fundamental limits and non-reciprocal approaches in non-Hermitian quantum sensing, Nat. Commun. **9**, 4320 (2018).
[31] S. Pirandola, B. R. Bardhan, T. Gehring, C. Weedbrook, and S. Lloyd, Advances in photonic quantum sensing, Nat. Photonics **12**, 724 (2018).
[32] L. Pezzè, A. Smerzi, M. K. Oberthaler, R. Schmied, and P. Treutlein, Quantum metrology with nonclassical states of atomic ensembles, Rev. Mod. Phys. **90**, 035005 (2018).
[33] A. McDonald and A. A. Clerk, Exponentially-enhanced quantum sensing with non-Hermitian lattice dynamics, Nat. Commun. **11**, 5382 (2020).
[34] H. Rudolph, U. C. V. Delić, M. Aspelmeyer, K. Hornberger, and B. A. Stickler, Force-gradient sensing and entanglement via feedback cooling of interacting nanoparticles, Phys. Rev. Lett. **129**, 193602 (2022).
[35] N. V. Lavrik and P. G. Datskos, Optically read Coriolis vibratory gyroscope based on a silicon tuning fork, Microsyst. Nanoeng. **5**, 47 (2019).
[36] M. Aspelmeyer, T. J. Kippenberg, and F. Marquardt, Cavity optomechanics, Rev. Mod. Phys. **86**, 1391 (2014).
[37] M. V. Gustafsson, T. Aref, A. F. Kockum, M. K. Ekström, G. Johansson, and P. Delsing, Propagating phonons coupled to an artificial atom, Science **346**, 207 (2014).
[38] M. J. A. Schuetz, E. M. Kessler, G. Giedke, L. M. K. Vandersypen, M. D. Lukin, and J. I. Cirac, Universal quantum transducers based on surface acoustic waves, Phys. Rev. X **5**, 031031 (2015).
[39] Y. Chu, P. Kharel, W. H. Renninger, L. D. Burkhart, L. Frunzio, P. T. Rakich, and R. J. Schoelkopf, Quantum acoustics with superconducting qubits, Science **358**, 199 (2017).
[40] R. Manenti, A. F. Kockum, A. Patterson, T. Behrle, J. Rahamim, G. Tancredi, F. Nori, and P. J. Leek, Circuit quantum acoustodynamics with surface acoustic waves, Nat. Commun. **8**, 975 (2017).
[41] Y. Chu, P. Kharel, T. Yoon, L. Frunzio, P. T. Rakich, and R. J. Schoelkopf, Creation and control of multi-phonon Fock states in a bulk acoustic-wave resonator, Nature **563**, 666 (2018).
[42] K. J. Satzinger, Y. P. Zhong, H.-S. Chang, G. A. Peairs, A. Bienfait, M.-H. Chou, A. Y. Cleland, C. R. Conner, E. Dumur, J. Grebel, I. Gutierrez, B. H. November, R. G. Povey, S. J. Whiteley, D. D. Awschalom, D. I. Schuster, and A. N. Cleland, Quantum control of surface acoustic-wave phonons, Nature **563**, 661 (2018).
[43] M. K. Ekström, T. Aref, A. Ask, G. Andersson, B. Suri, H. Sanada, G. Johansson, and P. Delsing, Towards phonon routing: Controlling propagating acoustic waves in the quantum regime, New J. Phys. **21**, 123013 (2019).
[44] G. Andersson, B. Suri, L. Guo, T. Aref, and P. Delsing, Non-exponential decay of a giant artificial atom, Nat. Phys. **15**, 1123 (2019).
[45] P. Delsing *et al.*, The 2019 surface acoustic waves roadmap, J. Phys. D: Appl. Phys. **52**, 353001 (2019).
[46] A. Noguchi, R. Yamazaki, Y. Tabuchi, and Y. Nakamura, Single-photon quantum regime of artificial radiation pressure on a surface acoustic wave resonator, Nat. Commun. **11**, 1183 (2020).

[47] S.-C. Wu, L. Zhang, J. Lu, L.-G. Qin, and Z.-Y. Wang, Surface-acoustic-wave-controlled optomechanically induced transparency in a hybrid piezo-optomechanical planar distributed Bragg-reflector-cavity system, Phys. Rev. A **103**, 013719 (2021).

[48] Y. T. Zhu, S. Xue, R. B. Wu, W. L. Li, Z. H. Peng, and M. Jiang, Spatial-nonlocality-induced non-Markovian electromagnetically induced transparency in a single giant atom, Phys. Rev. A **106**, 043710 (2022).

[49] Y. T. Zhu, R. B. Wu, Z. H. Peng, and S. Xue, Giant-cavity-based quantum sensors with enhanced performance, Front. Phys. **10**, 896596 (2022).

[50] L. Guo, A. Grimsmo, A. F. Kockum, M. Pletyukhov, and G. Johansson, Giant acoustic atom: A single quantum system with a deterministic time delay, Phys. Rev. A **95**, 053821 (2017).

[51] X.-L. Yin, W.-B. Luo, and J.-Q. Liao, Non-Markovian disentanglement dynamics in double-giant-atom waveguide-QED systems, Phys. Rev. A **106**, 063703 (2022).

[52] A. A. Clerk, M. H. Devoret, S. M. Girvin, F. Marquardt, and R. J. Schoelkopf, Introduction to quantum noise, measurement, and amplification, Rev. Mod. Phys. **82**, 1155 (2010).

[53] M. O. Scully and M. S. Zubairy, *Quantum Optics* (Cambridge University Press, Cambridge, 1997), p. 225.

[54] J. Schweer, D. Steinmeyer, K. Hammerer, and M. Heurs, All-optical coherent quantum-noise cancellation in cascaded optomechanical systems, Phys. Rev. A **106**, 033520 (2022).

[55] M. Koppenhöfer, C. Padgett, J. V. Cady, V. Dharod, H. Oh, A. C. Bleszynski Jayich, and A. A. Clerk, Single-spin readout and quantum sensing using optomechanically induced transparency, Phys. Rev. Lett. **130**, 093603 (2023).

[56] H. Vahlbruch, M. Mehmet, K. Danzmann, and R. Schnabel, Detection of 15 dB squeezed states of light and their application for the absolute calibration of photoelectric quantum efficiency, Phys. Rev. Lett. **117**, 110801 (2016).